Focus Section: Data Mine: 2019 Ridgecrest, California Earthquake Sequence

Rapid Geodetic Observations of Spatiotemporally Varying Postseismic Deformation Following the Ridgecrest Earthquake Sequence: The U.S. Geological Survey Response

Benjamin A. Brooks[*1], Jessica Murray[1], Jerry Svarc[2], Eleyne Phillips[2], Ryan Turner[2], Mark Murray[2], Todd Ericksen[2], Kang Wang[3], Sarah Minson[1], Roland Burgmann[3], Fred Pollitz[1], Ken Hudnut[4], Johanna Nevitt[1], Evelyn Roeloffs[5], Janis Hernandez[6], and Brian Olson[6]

Abstract

The U.S. Geological Survey's geodetic response to the 4–5 July 2019 (Pacific time) Ridgecrest earthquake sequence comprised primarily the installation and/or reoccupation of Global Navigation Satellite System (GNSS) monumentation. Our response focused primarily on the United States' Navy's China Lake Naval Air Weapons Station base (NAWSCL). This focus was because much of the surface rupture occurred on the NAWSCL and because of NAWSCL access restrictions only permitting Federal and State of California personnel. In total, we measured or are still measuring at 24 sites, 14 of which were on the NAWSCL and, as of this writing, operational. The majority of sites were set up as continuous stations logging at either 1 sample per second or 1 sample per 15 s. Two stations were recording a 200 m cross-rupture aperture starting ∼10 hr after the *M* 6.4 event, and they recorded the coseismic displacements of the *M* 7.1. Approximately, 1 hr after the *M* 7.1 event, two new stations were recording a ∼200 m cross-rupture aperture of the surface rupture. In the days following, we established the rest of the stations ranging to a distance of ∼15 km from the *M* 7.1 principal rupture trace. The lack of differential displacement across the *M* 6.4 rupture during the *M* 7.1 event suggests that it did not reactivate the *M* 6.4 plane. The lack of differential cross-fault displacement for both events suggests that rapid shallow afterslip did not occur at those two locations. The postseismic time series from these stations shows centimeters of horizontal displacement over periods of a few months. They record a mixture of fault-parallel and fault-normal displacements that, in conjunction with analysis of more spatially complete Interferometric Synthetic Aperture Radar displacement fields, suggest that both poroelastic and afterslip phenomena occur along the *M* 6.4 and 7.1 rupture planes. Using preliminary data from these and other regional stations, we also explore the Ridgecrest sequence's effect on regional GNSS time series and the differentiation of long-term postseismic motions and secular deformation rates. We find that redefining a common-mode noise filter using different GNSS stations that are assumed to be unaffected by the earthquakes results in small but systematic differences in the regional velocity field estimate.

Cite this article as Brooks, B. A., J. Murray, J. Svarc, E. Phillips, R. Turner, M. Murray, T. Ericksen, K. Wang, S. Minson, R. Burgmann, *et al.* (2020). Rapid Geodetic Observations of Spatiotemporally Varying Postseismic Deformation Following the Ridgecrest Earthquake Sequence: The U.S. Geological Survey Response, *Seismol. Res. Lett.* **XX**, 1–16, doi: 10.1785/0220200007.

Supplemental Material

Introduction

The southern California 2019 Ridgecrest earthquake sequence from 4 to 5 July (Pacific time) was a multifault rupture comprising a left-lateral *M* 6.4 foreshock (∼11.7 km depth) on a northeast-trending fault plane followed ∼34 hr later by a right-lateral *M* 7.1 (∼8 km depth) mainshock on a

1. Earthquake Science Center, U.S. Geological Survey, Moffett Field, California, U.S.A.; 2. Earthquake Science Center, U.S. Geological Survey, Menlo Park, California, U.S.A.; 3. Department of Earth and Planetary Science, University of California, Berkeley, Berkeley, California, U.S.A.; 4. Earthquake Science Center, U.S. Geological Survey, Pasadena, California, U.S.A.; 5. Earthquake Science Center, U.S. Geological Survey, Vancouver, Washington, U.S.A.; 6. California Geological Survey, Los Angeles, California, U.S.A.

*Corresponding author: bbrooks@usgs.gov

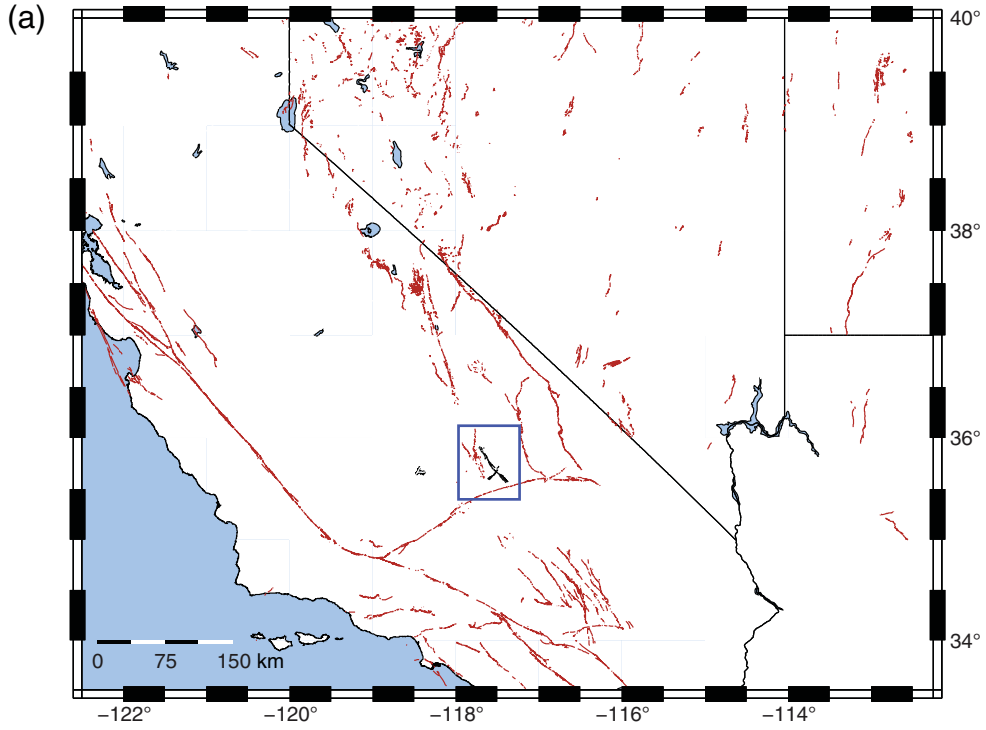

Figure 1. (a) Regional location map showing western U.S. state boundaries and mapped Quaternary fault traces (red lines). The blue box indicates the study area and Ridgecrest earthquakes surface rupture (black lines) shown in (b). (b) Study area showing the city of Ridgecrest, location of the China Lake Naval Air Weapons Station base (NAWSCL) (cyan lines), mapped Quaternary faults (pink lines), the Ridgecrest earthquake sequence surface rupture trace (red lines, C. B. DuRoss *et al.*, unpublished manuscript, see Data and Resources), Plate Boundary Observatory continuous stations (yellow squares), and stations installed or occupied as part of this study (green squares). Red vectors are coseismic displacements estimated for the M 7.1 event. Note that displacements from stations RCRW and RCRE are so similar, they plot on top of one another. GF, Garlock fault; LLFZ, Little Lake fault zone; SNFZ, Sierra Nevada fault zone. Stations RCRW and RCRE as well as 71RW and 71RE are along Highway 178. Spray-paint markers discussed in the Instrument Deployment and Details section were installed between each of these two locations.(*Continued*)

northwest-trending fault plane (Ross *et al.*, 2019; Stewart *et al.*, 2019) (Fig. 1a). Both events produced substantial surface rupture (~1–5 m) measured over distances of 10s of kilometers (Stewart *et al.*, 2019). Although previously unmapped, the causative faults reside in the Little Lake fault zone, a northwest-trending series of faults that occur in a complicated portion of the Eastern California Shear Zone (ECSZ) that is ~25 km east of the southern terminus of the southern Sierra Nevada fault zone (itself the western limit of Basin and Range extension) and ~15 km north of the east-northeast–west-southwest-trending left-lateral Garlock fault. As a result of this setting, the region experiences a complicated background combination of right-lateral ECSZ-related stress, extensional stress from Basin and Range deformation, and left-lateral, Garlock-related stress (Becker *et al.*, 2005). Given that it was the first major seismic event in southern California for two decades, the Ridgecrest sequence generated a substantial amount of scientific interest and research. Early reports have focused on the surface disruption (Stewart *et al.*, 2019) and multifault nature of the sequence (Ross *et al.*, 2019).

Here, we report on the rapid geodetic response to the Ridgecrest sequence led by the U.S. Geological Survey (USGS). Much of the surface rupture for both events occurred within the limits of the United States' Navy's China Lake Naval Air Weapons Station base (NAWSCL). Because of NAWSCL access restrictions, USGS and California Geological Survey personnel were the only scientists permitted onsite and to deploy equipment. Immediately following the M 6.4 event, our team maintained close contact and collaboration with the large group of academic geodetic researchers from the Southern California Earthquake Center (SCEC) (Floyd *et al.*, 2020).

Our principal scientific objective is to better understand postseismic deformation processes—both the surface deformation they produce and, through inference, the physical processes controlling slip on the fault planes. The spatiotemporal signatures of different postseismic processes such as poroelastic rebound and dilation (Peltzer *et al.*, 1996), fault afterslip (Marone *et al.*, 1991), and viscoelastic relaxation (Pollitz *et al.*, 2001; Bürgmann and Dresen, 2008) are fundamental characteristics of continental lithosphere that can only be studied following infrequent seismic events. The postseismic response to crustal faulting still poses first-order questions: what is the relative contribution of fault afterslip versus viscoelastic mantle relaxation? When and why do poroelastic postseismic responses occur? Why do some faults have shallow afterslip and others not? For instance, the large amount of shallow, rapid afterslip for the M_w 6.0 South Napa earthquake was a surprise (Floyd *et al.*, 2016; Brooks *et al.*, 2017). The shallowest portion of seismogenic faults (<1 km depth) has gained much recent attention, in particular, because of the significant increase in sensing capability for near-field surface

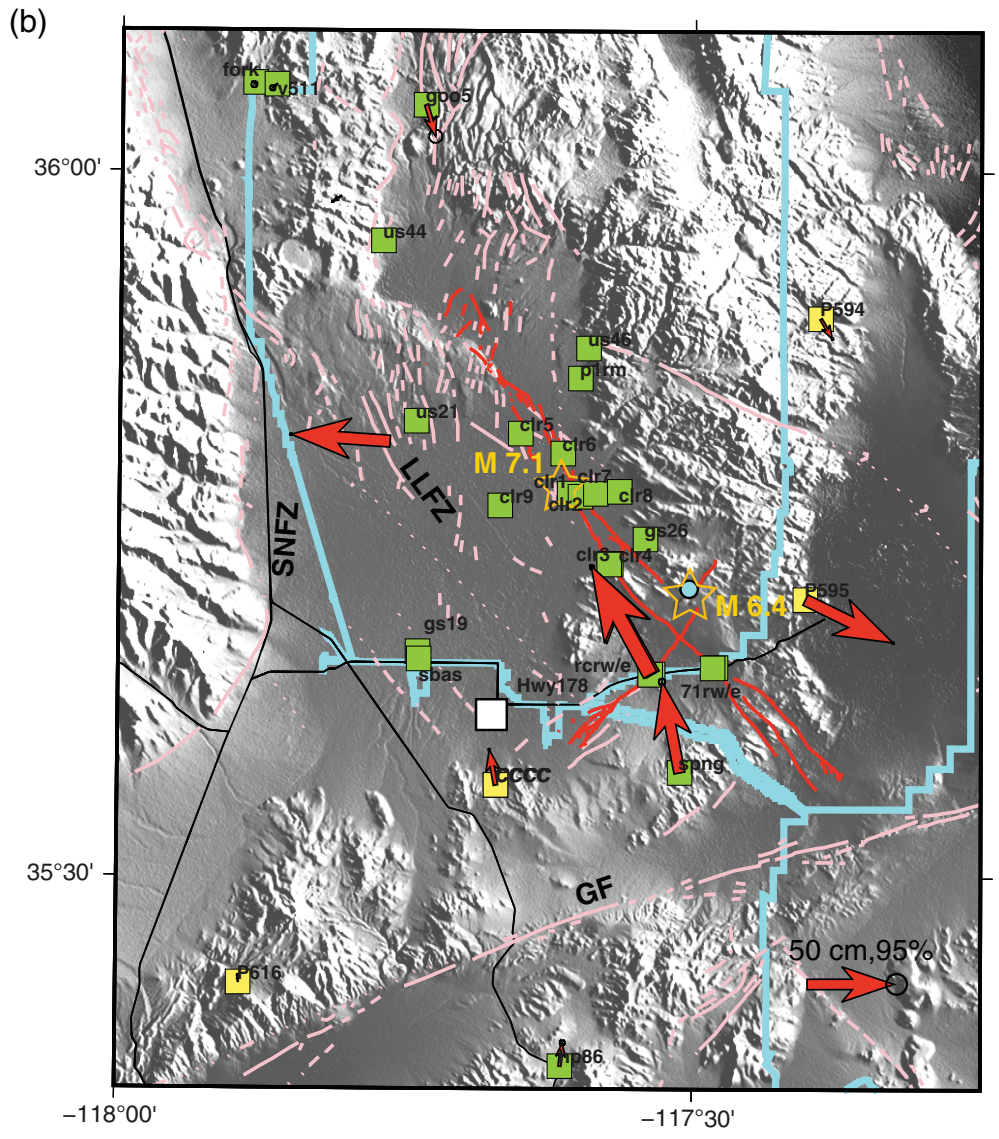

Figure 1. Continued

deformation (Nissen *et al.*, 2014; Zinke *et al.*, 2014; Milliner *et al.*, 2015; Brooks *et al.*, 2017). Given that historical surface ruptures predominate in the databases from which empirical relations for seismic hazard analyses are derived (Wesnousky, 2008), it is important to document the prevalence of rapid shallow afterslip. In addition, the presence or absence of rapid shallow afterslip (occurring minutes to days after the mainshock) is critical to the current debate about the amount of coseismic slip that reaches the surface in continental strike-slip faulting events (Simons *et al.*, 2002; Fialko *et al.*, 2005; Dolan and Haravitch, 2014; Xu *et al.*, 2016) and whether a deficit in shallow coseismic slip could be rapidly recuperated by afterslip, as it was, for instance in the 2004 M_w 6.0 Parkfield earthquake (Bilham, 2005; Langbein *et al.*, 2006) and the South Napa event (Lienkaemper *et al.*, 2016; Brooks *et al.*, 2017). Robust quantification of the postseismic deformation field both in the near- and far field of faults also potentially permits placing rheological constraints on the shallowest portion of slipping faults for which, recently, there has been much interest, especially in the field of fault displacement hazard analysis (Petersen *et al.*, 2011).

To address these questions, it is critical to rapidly collect geodetic data on surface deformation, especially in the near field. Although space-based instruments have the capability of widespread imaging, their response time (days) is not necessarily adequate to capture the afterslip decay that occurs hours to days after the mainshock (Marone *et al.*, 1991; Aagaard *et al.*, 2012). Until more ubiquitous space-based imaging is available, we must rely on field efforts.

As described subsequently, the USGS Earthquake Science Center (ESC) team mobilized immediately after the 4 July M 6.4 Ridgecrest event and began making geodetic measurements by 08:00 p.m. on 4 July (Pacific time). The team was onsite for the 5 July (Pacific time) M 7.1 event and began making measurements immediately. Accordingly, some of the postseismic geodetic data sets presented here are among the most rapidly collected datasets for continental surface-rupturing earthquakes (Floyd *et al.*, 2016). Moreover, the data that were collected are unique because of their location surrounding the epicentral region and zone of maximum surface rupture and their proximity to the inferred portions of maximum slip on the M 7.1 fault plane.

In addition to rapid response activities, USGS-ESC has also implemented an automated system for regional Global Navigation Satellite System (GNSS) data processing and time-series analysis (Murray and Svarc, 2017). Each day the system incorporates newly available observations from permanent networks and campaign deployments to update position time series and constant velocity estimates for stations

throughout the western United States. To reduce common-mode error prior to velocity estimation, we divide the western United States into regions and follow the method of Blewitt *et al.* (2013). This approach uses a small number of continuous GNSS stations distributed throughout the region to define a regional filter that can be applied to time series from any other site in the region. The stations defining the filter are selected to have long time series that exhibit low scatter and minimal transient motion. The Ridgecrest sequence caused significant coseismic and ongoing postseismic displacements at regional continuously operating and campaign GNSS stations. The displacements have the potential to affect velocity estimates both through region-wide reference frame adjustments and in the estimation of velocities for individual stations. Thus, an added aspect of our work presented here is to quantify and mitigate any effect that Ridgecrest-related (co- or postseismic) deformation could have on the reliability of GNSS data products distributed by the USGS.

Instrument Deployment and Details

Because the logistics and technology of earthquake rapid response are continuously evolving, we present here, as detailed as possible, a timeline of USGS response events. See Figure 1 for key geographic references and station locations and Table 1 for a list of station names, measurement dates, and sample frequencies.

4 July

The *M* 6.4 event occurred on 4 July at 17:33 UTC (10:33 Pacific time). Within minutes, USGS deformation team members had received parameters from the event from the USGS Earthquake Notification System (see Data and Resources) and had begun postevent coordination. Based on the size and relatively shallow hypocentral depth, it was assumed that there would likely be surface rupture and a postseismic geodetic signal associated with the event. The coordination was complicated by the fact that the event occurred on the 4 July United States national holiday, and most personnel were on vacation leave. Despite this, however, three of our team members were able to deploy within 1–2 hr (Brooks from Truckee, California; Ericksen from Menlo Park, California; and Hudnut from Pasadena, California) and two others (Svarc and Phillips) deployed from Menlo Park, California later in the afternoon of 4 July.

By the time the two teams met in Ridgecrest at 07:45 p.m. (Pacific time), significant surface faulting had been observed and confirmed 1 hr previously on Highway 178 by our team members (Hudnut and Hernandez). With the remaining sunlight of 4 July, the two teams visited the surface rupture crossing Highway 178 and began the geodetic deployment. We installed one GNSS station ~100 m either side of the principal expression of the *M* 6.4 surface rupture (Fig. 1 and Table 1, sites RCRW, RCRE). No pre-existing survey monuments existed near the surface rupture, so the antennae was centered over survey stakes driven into the sand. In addition, we spray-painted marks orthogonal to coseismic fractures on the Highway 178 pavement to assess the presence or absence of shallow afterslip (Fig. 2). At the Highway 178 rupture crossing, we also met and coordinated with the SCEC field team who had focused on reoccupying pre-existing geodetic benchmarks off the NAWSCL (led by G. Funning, Floyd *et al.*, 2020).

5 July

At 05:00 a.m. the morning of 5 July, based on the illumination of the northwest-striking plane by the vigorous aftershock sequence from the *M* 6.4 event, one of us (Brooks) checked to see if there was any surface manifestation of faulting at the surface projection of the northwest-striking plane and Highway 178 (Fig. 1). This consisted of driving the entire road from Ridgecrest to Trona, as well as on-foot reconnaissance of the expected intersection of the northwest plane and Highway 178. We found no evidence of surface disruption.

In coordination with the SCEC team, Svarc and Phillips began to reoccupy pre-existing geodetic monuments outside of NAWSCL limits (Fig. 1 and Table 1), whereas Brooks and Ericksen conducted mobile laser scanning of the off-base surface rupture, and Hudnut and Hernandez established contact with NAWSCL base leadership and conducted the initial on-base reconnaissance of *M* 6.4 surface rupturing.

At 08:19 Pacific time (03:19 UTC 6 July), the entire team was beginning a California Earthquake Clearinghouse (see Data and Resources) meeting at the Ridgecrest City Hall when the *M* 7.1 mainshock occurred. After following drop, cover, and hold-on protocol (Fig. 3) and assuring personal safety of all team members, we were informed via text message from a USGS colleague (Elizabeth Cochran, written comm., 2019) that it appeared the *M* 7.1 event had activated the northwest-striking plane previously illuminated following the 4 July *M* 6.4 event (Fig. 1). Given this information, Brooks, Ericksen, Phillips, and Olson headed east on Highway 178 to the same site Brooks had checked earlier that morning. There we found substantial right-lateral surface rupture (Fig. 4a) exceeding ~1 m. Similar to sites RCRW and RCRE, we installed one GNSS site within ~100 m of each side of the zone of surface rupture disrupting Highway 178 (71RW and 71RE). No pre-existing survey monuments existed near the surface rupture, so the antennae was again centered over survey stakes driven into the sand. In addition, we made measuring tape displacement measurements and spray-painted orthogonal marks across right-lateral surface fractures (Fig. 4b).

6 July

Because the *M* 7.1 mainshock occurred so close to sundown on 5 July (Pacific time), 6 July was the first day that permitted first-order reconnaissance of the principal surface rupture. Accordingly, for the teams permitted on the NAWSCL, the priority was first-order helicopter-based field reconnaissance of the principal surface rupture. Because the reconnaissance

TABLE 1
GNSS Sites and Occupation Metrics

Station Name	Latitude (°)	Longitude (°)	First (yyyy/mm/dd)	Most Recent (yyyy/mm/dd)	Receiver	Antenna	Frequency A	Frequency B
3187	36.02325362	−118.1356627	1993/08/14	2019/08/14	TURBOROGUE 93.06.08	AOAD/M_T	15 s	
6813	36.15039275	−117.6752477	1994/11/21	2019/09/20	ASHTECH LM-XII3	ASH700228A	15 s	
71re	35.64903117	−117.4806849	2019/07/06	2019/07/08	JAVAD TRE_G3TH SIGMA3.7.6	JAVRINGANT_DM	15 s	
71rw	35.64887895	−117.4832135	2019/07/06	2019/07/08	JAVAD TRE_G3TH SIGMA3.7.6	JAVRINGANT_DM	15 s	
clr1	35.7722234	−117.6082856	2019/07/06	2020/03/03	JAVAD TRE_G3TH SIGMA3.7.6	JAVRINGANT_DM	15 s	1 s
clr2	35.77008852	−117.5988909	1992/08/03	2020/02/24	JAVAD TRE_G3TH SIGMA3.7.6	JAVRINGANT_DM	15 s	1 s
clr3	35.72264251	−117.5721275	2019/07/05	2020/03/02	JAVAD TRE_G3TH SIGMA3.7.6	JAVRINGANT_DM	15 s	1 s
clr4	35.72206761	−117.5735844	2019/07/06	2020/03/02	JAVAD TRE_G3TH SIGMA3.7.6	JAVRINGANT_DM	15 s	1 s
clr5	35.81458737	−117.6511545	2019/07/28	2020/01/21	TRIMBLE NETR9	TRM57971.00	15 s	`
clr6	35.80059226	−117.6141589	2019/09/11	2020/01/21	TRIMBLE NETR9	TRM57971.00	15 s	1 s
clr7	35.77215098	−117.5855546	2019/07/29	2020/01/21	TRIMBLE NETR9	TRM57971.00	15 s	1 s
clr8	35.77368375	−117.5646928	2019/07/31	2020/01/21	TRIMBLE NETR9	TRM57971.00	15 s	1 s
clr9	35.76348415	−117.668663	2019/08/01	2019/11/29	TRIMBLE NETR9	TRM57971.00	15 s	1 s
Fork	36.06246854	−117.8843298	1992/02/26	2020/01/25	ASHTECH LM-XII3	ASH700228A	15 s	
goo5	36.04729365	−117.7353311	1994/11/20	2019/09/20	ASHTECH Z-XII3	ASH700228D	15 s	
gs19	35.65974347	−117.7396535	2019/07/19	2020/03/01	JAVAD TRE_G3TH	JAVRINGANT_DM	15 s	1 s
gs26	35.74005377	−117.542011	2019/07/06	2020/03/02	JAVAD TRE_G3TH	JAVRINGANT_DM	15 s	1 s
hp86	35.36616153	−117.6142056	1994/03/19	2019/07/08	ASHTECH LM-XII3	ASH700228A	15 s	
Jbon	35.33621752	−117.9956617	1994/03/18	2019/09/15	ASHTECH LM-XII3	ASH700228A	15 s	
l166	36.27913113	−117.549881	1994/11/19	2019/09/15	ASHTECH Z-XII3	ASH700228A	15 s	
p166	36.3069368	−117.6409749	1993/08/14	2019/09/14	TURBOROGUE 93.06.08	AOAD/M_T	15 s	
p1rm	35.85388023	−117.5990811	2019/08/01	2020/01/21	TRIMBLE NETR9	TRM55971.00	15 s	
Rcre	35.64436215	−117.5353142	2019/07/05	2019/07/08	JAVAD TRE_G3TH SIGMA3.7.6	JAVRINGANT_DM	15 s	
Rcrw	35.64410227	−117.5373409	2019/07/05	2019/07/31	JAVAD TRE_G3TH SIGMA3.7.6	JAVRINGANT_DM	15 s	
Sbas	35.65464391	−117.7386526	2019/07/11	2019/07/18	JAVAD TRE_G3TH SIGMA3.7.6	JAVRINGANT_DM	15 s	
Spng	35.57457234	−117.5114493	1994/03/18	2019/09/14	ASHTECH LM-XII3	ASH700228A	15 s	
us21	35.82322171	−117.7418649	2019/07/27	2020/01/22	TRIMBLE NETR9	TRM57971.00	15 s	

Station name, latitude, longitude: site code and coordinates. First, most recent: dates of first and most recent occupations in eight digit code of year (characters 1–4), month (characters 5–6), day (characters 7–8). Receiver, antenna: receiver and antenna types. Frequency A, B: sampling frequencies. GNSS, Global Navigation Satellite System.
(Continued next page.)

TABLE 1 (continued)
GNSS Sites and Occupation Metrics

Station Name	Latitude (°)	Longitude (°)	First (yyyy/mm/dd)	Most Recent (yyyy/mm/dd)	Receiver	Antenna	Frequency A	Frequency B
us44	35.95088078	−117.7716213	2019/07/27	2020/01/22	TRIMBLE NETR9	TRM57971.00	15 s	
us46	35.87512901	−117.5921808	2019/07/27	2019/11/18	TRIMBLE NETR9	TRM57971.00	15 s	1 s
v511	36.06142017	−117.8656792	1994/11/21	2019/07/08	ASHTECH LM-XII3	ASH700228D	15 s	

Station name, latitude, longitude: site code and coordinates. First, most recent: dates of first and most recent occupations in eight digit code of year (characters 1–4), month (characters 5–6), day (characters 7–8). Receiver, antenna: receiver and antenna types. Frequency A, B: sampling frequencies. GNSS, Global Navigation Satellite System.

focused on the surface rupture, we were able to place three GNSS stations relatively near the principal surface rupture. One of the stations, GS26 was a reoccupation of a pre-existing benchmark. In addition, we established two new stations, CRL1 and CRL2, straddling the principal surface rupture near the epicentral region. Outside of NAWSCL borders, we also reoccupied stations SPNG and JBON.

7–11 July

We concentrated on reoccupying stations outside of NAWSCL borders: HP86 (7/7), FORK (7/9), and SBAS (7/11).

28 July–1 August

We conducted a follow-on campaign during this time to download data and to reoccupy and establish new stations with the simultaneous objectives of the Ridgecrest postseismic science goals (as discussed in the Introduction) as well as to provide navigational control for the joint USGS–SCEC airborne laser scanning (ALS) survey of the principal rupture zone (Hudnut *et al.*, 2020). Generally, the stations established farther from the rupture trace (US21, US44, US46, and previously established GS26 and GS19) were also used for the ALS navigation control. The stations established closer to the rupture trace (CLR5, CLR6, CLR7, CLR8, and CLR9; because of equipment issues, CLR6 did not record data until 9/11) were established to capture the near-field postseismic displacement field.

An important aspect of this deployment is that, because the spatiotemporal nature of the near-field postseismic signal was rapidly evolving, we sited stations based on near-real-time interaction with teams from University of California, Berkeley (Wang and Bürgmann, 2020), and Jet Propulsion Laboratory (Eric Fielding, written comm., 2019) that were analyzing Sentinel-1 and Cosmo–SkyMed Interferometric Synthetic Aperture Radar (InSAR) displacement fields from the region (Fig. 5). This helped, in particular, in siting stations CLR5, CLR6, CLR7, CLR8, and CLR9.

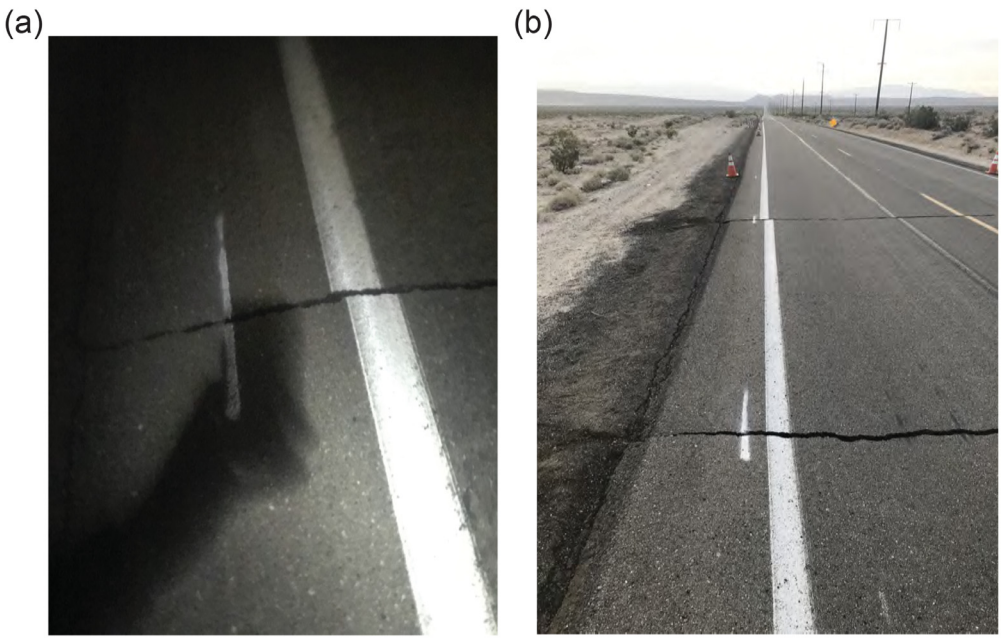

Figure 2. Photos of the M_w 6.4 surface rupture crossing Highway 178 and of spray-paint markers across individual shear fractures. All photos are looking east. See Figure 1b, stations RCRW and RCRE for location. (a) Photo taken at 09:04 p.m. (Pacific time) on 4 July. (b) Photo taken at 06:05 a.m. (Pacific time) on 7 July. The lack of displacement across the spray-paint markers indicates no differential motion took place at that location.

10–14 September

We reoccupied existing sites P166 (9/10), G005 (9/12), and L166 (9/14).

Instrumentation

Our GNSS equipment comprises USGS and UNAVCO-provided instrumentation (Fig. 6). Each site consists of a receiver, antenna, tripod with tribrach, and power system usually including a 12 V

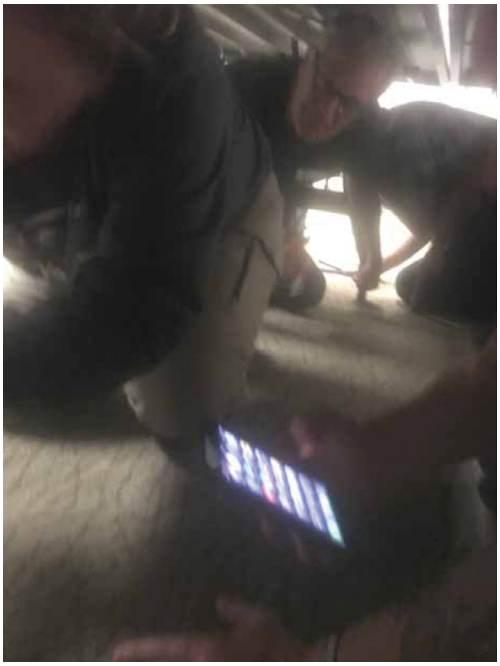

Figure 3. Team personnel following drop–cover–hold on protocol at Ridgecrest City hall during *M* 7.1 mainshock. See Figure 1b for Ridgecrest location. Time of photo was 08:20:12 (Pacific time).

battery and solar panels. USGS instrumentation consists of a Javad SIGMA Global Positioning System (GPS) receiver with a choke-ring antenna. UNAVCO instrumentation consists of a Trimble NetR9 receiver and Trimble Zephyr 2 GNSS antenna. Upon setup, the receivers were enclosed in their Pelican travel cases with pass-throughs for power and GNSS cabling. Most of the sites were outfitted with steel frames for the solar panels. The frames were designed to maximize power output, prevent movement in high winds, and to provide some shade for the campaign equipment below them. Generally, because of on-base explosive hazard and environmental concerns, we were not granted permission to dig holes to bury the equipment. Most stations were set to run at 1 sample per second, though some were collecting data at rates of 1 sample per 15 s (Table 1).

Overall Data Quality and Availability

All data and associated metadata are available as standard Reciever Independent Exchange Format files at the UNAVCO archive (see Data and Resources). Because of the rapid nature of the response and the extreme temperatures encountered in the field (days were routinely above 40°C for many hours), data continuity on some of the sites was sporadic. Data quality at each of the sites, in general, is excellent. The only station with a known data issue is US46, which was found to be off-centered and out of level on 20 September. A GNSS processing tie was done on that day to translate the position of US46 to P1RM. Despite the data outages, the data are of sufficient quality to create daily solutions that clearly show postseismic trends of 10s of millimeters over a period of months.

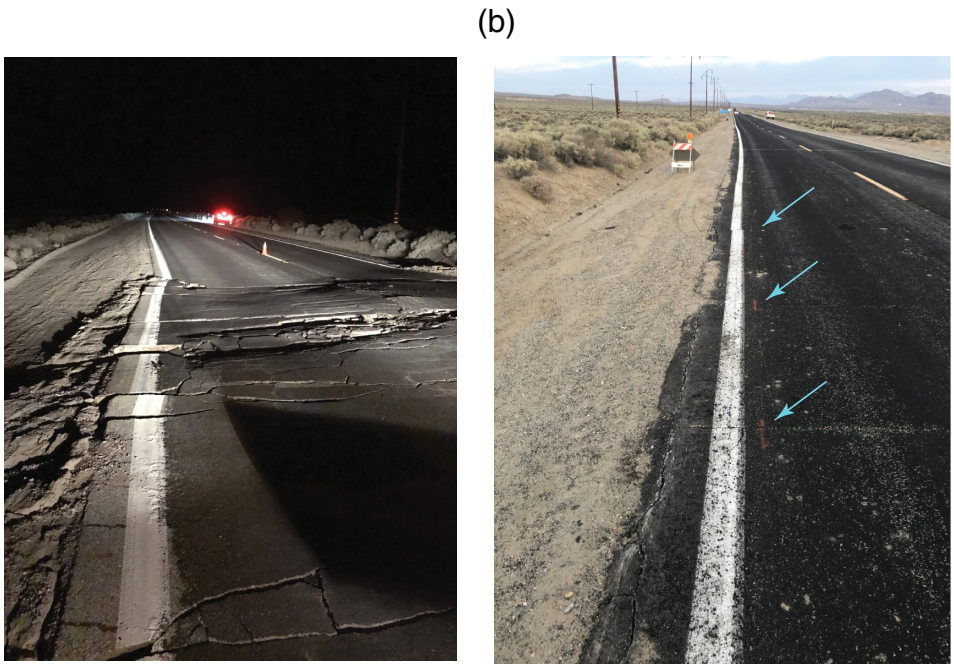

Figure 4. Photos of the M_w 7.1 surface rupture crossing Highway 178. See Figure 1b, stations 71RW and 71RE for location. All photos are looking west. (a) Photo taken at 10:19 p.m. (Pacific time) on 5 July showing meter scale right-lateral offset of Highway 178. (b) Photo taken at 05:57 a.m. (Pacific time) on 7 July. The lack of displacement across the spray-paint markers (cyan arrows) indicates no differential motion took place at that location.

Initial Observations

The displacements recorded by these stations will be used to help quantify the nature of both co- and postseismic processes for the Ridgecrest earthquake sequence. Because station distance from the rupture planes range from 100s of meters to 10s of kilometers, they provide a range of surface observations that are sensitive to slip at depths of 100s of meters to 10 kilometers on the causative fault planes. Furthermore, the stations crossing Highway 178 can be

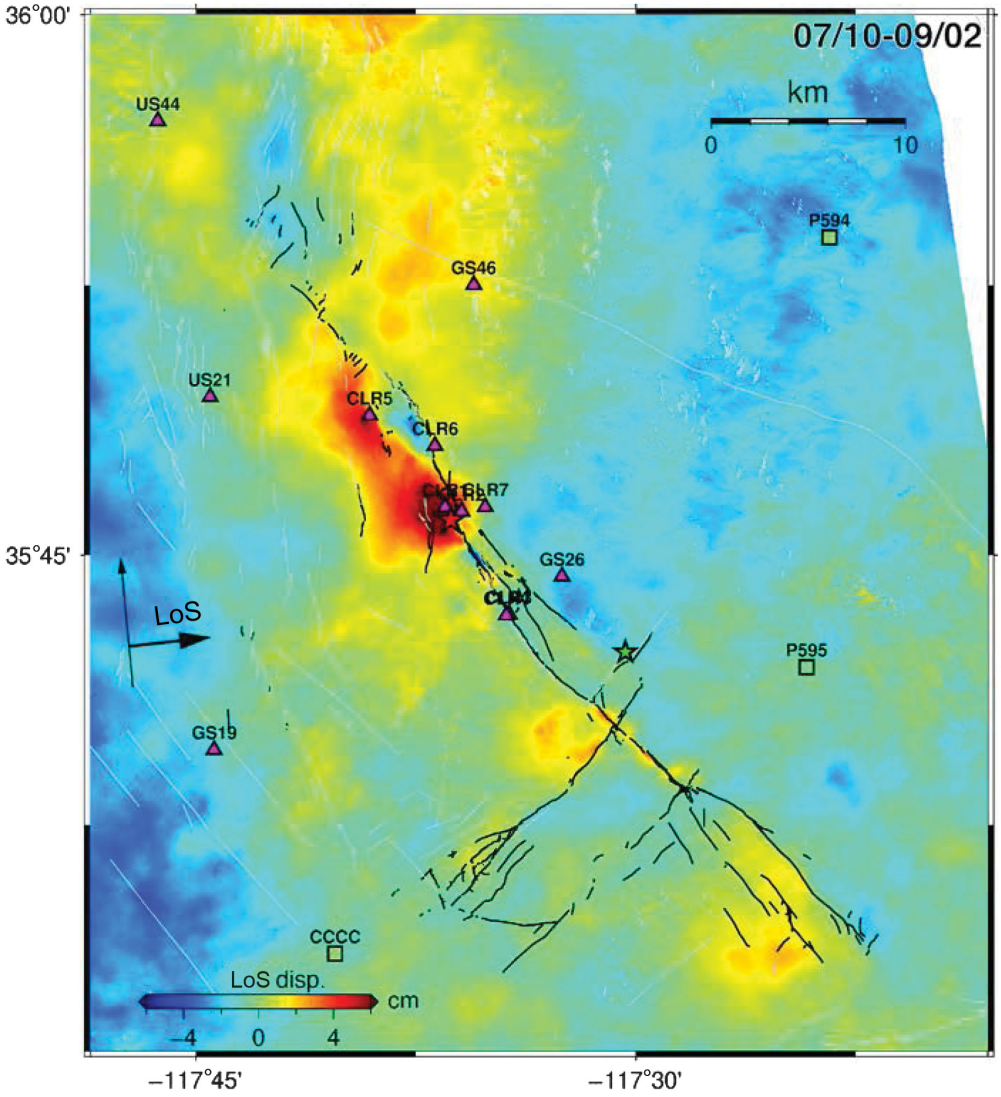

Figure 5. Cumulative Sentinel-1 line of sight displacements from 10 July to 2 September 2019 from (Wang and Bürgmann, 2020). Station pairs RCRW–RCRE and 71RW–71RE are not shown, as they were removed a few days after the installations. LoS, line of sight.

used to investigate the presence or absence of rapid shallow postseismic processes, whereas all the other stations will be used to distinguish different mechanical processes causing continuing postseismic deformation. This could include fault afterslip, poroelastic response of the shallow crust, and deeper viscoelastic relaxation in the lower crust and upper mantle.

Subsequently, we describe initial observations following roughly the chronological order in which the stations were constructed. The results are from both kinematic and daily solution processing.

Our automated daily processing is described elsewhere (Murray and Svarc (2017)). The kinematic results are 5 min kinematic positions using GIPSY-OASIS software version 6.3 (v.6.3). The kinematic results are calculated by first doing a kinematic estimate of the station position and changes in the troposphere using a random walk constraint. The tropospheric delay estimates are then used in the final kinematic estimate to determine the best solution.

The two stations on either side of the *M* 6.4 rupture at Highway 178, RCRW, and RCRE showed no differential motion across the fault plane from the evening of 4 July (Pacific time) to the *M* 7.1 occurrence on the evening of 5 July (Pacific time, Fig. 7a). For the *M* 7.1 rupture, however, they both recorded northwest static displacements of close to 70 cm—because these stations were the closest to the zone of maximum slip, these measurements represent the largest observed coseismic displacements for the event (Fig. 1b and see The Effect of the Ridgecrest Earthquakes on Automated daily GNSS Analysis section). Moreover, a vector difference of the static displacements for the *M* 7.1 event shows negligible across-fault displacement and indicates that the *M* 6.4 rupture plane was not activated in this location (at least the shallow part of it), during the *M* 7.1 event.

The two stations on either side of the *M* 7.1 rupture at Highway 178, 71RW, and 71RE are also showed no differential motion across the fault plane for the 3 days following the *M* 7.1 event (Fig. 7b). Because of CalTrans road repair activity, these stations were taken down after 3 days of operation.

The remainder of all the stations clearly indicate significant postseismic displacements. We present these observations both as individual time series (Fig. 8, see supplemental material) and as a plot of cumulative displacements (Fig. 9). Generally, on the east side of the fault, horizontal displacements are southeast-directed and subparallel to the trend of the *M* 7.1 rupture (e.g., stations CLR1, CLR2, and GS26, Figs. 8a–c and 9). These stations follow a roughly time-invariant trajectory. On the west side of the fault, most of the displacements are northwest-west-directed with a significant fault-normal component. In

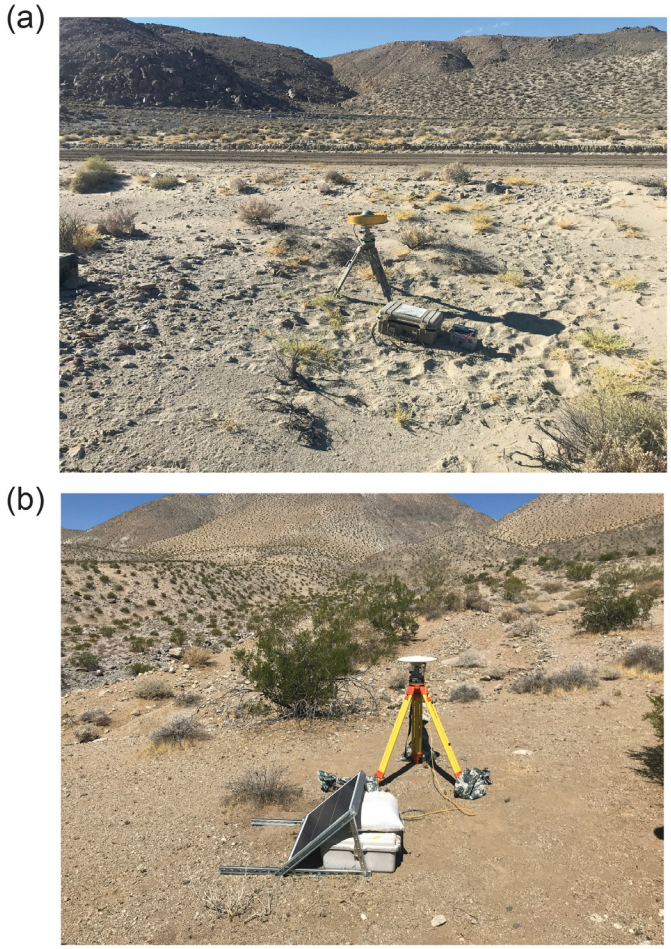

Figure 6. Photos of Global Navigation Satellite System (GNSS) instrumentation. (a) U.S. Geological Survey (USGS) instrumentation, site CLR1. (b) UNAVCO instrumentation, site US44.

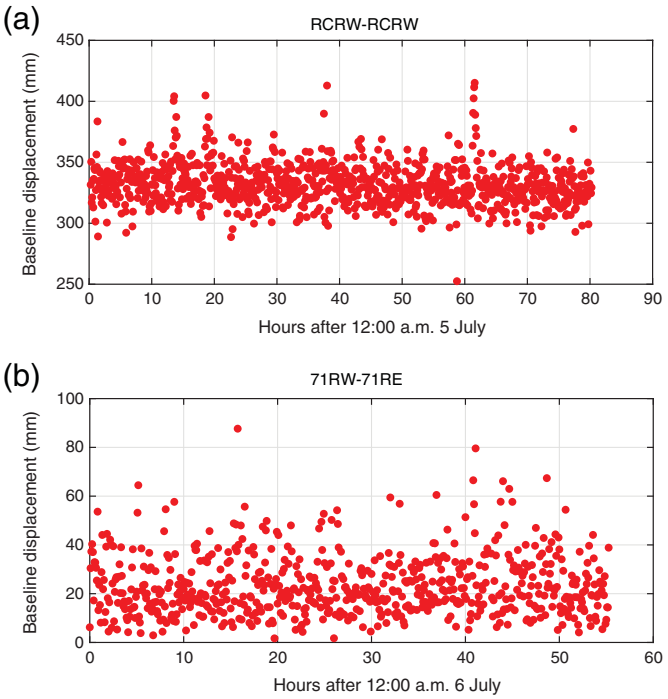

Figure 7. Results of kinematic processing for stations straddling ruptures across Highway 178. Note different *y*-axis scaling in each figure. (a) Differential three-component baseline of stations RCRW–RCRE, starting on 5 July 2019. (b) Differential three-component baseline of stations 71RW–71RE, starting on 6 July 2019.

contrast to the stations on the east side of the fault, three of these stations, however, show a time-variant trajectory. The time variance is particularly notable in the time series for station US44 (Fig. 8d), which shows a clear transient excursion in the north and east components, ~3 cm and ~5 mm, respectively, from day ~225–230 to day 250. Horizontal and vertical repeatabilities in the time-series data are on the order of ~2–4 mm and ~4–6 mm, respectively, so transient motion on the order of ~1 cm should be clearly detectable. Moreover, we are confident that this is not a site effect at U44 (such as monument movement) because the excursion is present at CLR5 (Fig. 8e) and CLR9 (Fig. 8f). At CLR5, the excursion manifests itself as a reversal in the north-component's displacement from south- to north-directed at ~day 230. At CLR9, the excursion manifests as a cessation of south-directed displacement at ~day 230.

The largest observed postseismic vertical displacements are in the epicentral region where stations CLR1 (Fig. 8a) and CLR2 (Fig. 8b) display ~4 cm of cumulative uplift. The CLR2 vertical time series suggests an initial period of downward motion of close to ~2 cm over the first ~20 days postevent. Generally, the observed cumulative vertical displacements are consistent with the pattern of uplift seen in the cumulative postseismic InSAR displacement field (Fig. 5).

Initial Postseismic Results

The results from our rapid deployment permit us to put some first-order constraints on the behavior of both the *M* 6.4 and 7.1 rupture planes during and after the *M* 7.1 event.

The observations from the first-established stations along Highway 178 place a strong constraint on the behavior of the *M* 6.4 northeast-trending rupture plane during the M_w 7.1 event. Stations RCRW (70.1 cm magnitude) and RCRE (69.2 cm magnitude) moved almost identical to the northwest, consistent with right-lateral motion on the *M* 7.1 rupture plane (Fig. 1b). We consider the ~9 mm vector difference between the two to be negligible. Combined with the lack of any evidence for surface disruption from our spray-paint markers (Fig. 2), we find no evidence that the *M* 6.4 rupture plane was reactivated during the *M* 7.1 event.

The *M* 7.1 postseismic displacements allow us to place a first-order observational constraint on the spatiotemporal variability of postseismic faulting processes associated with the

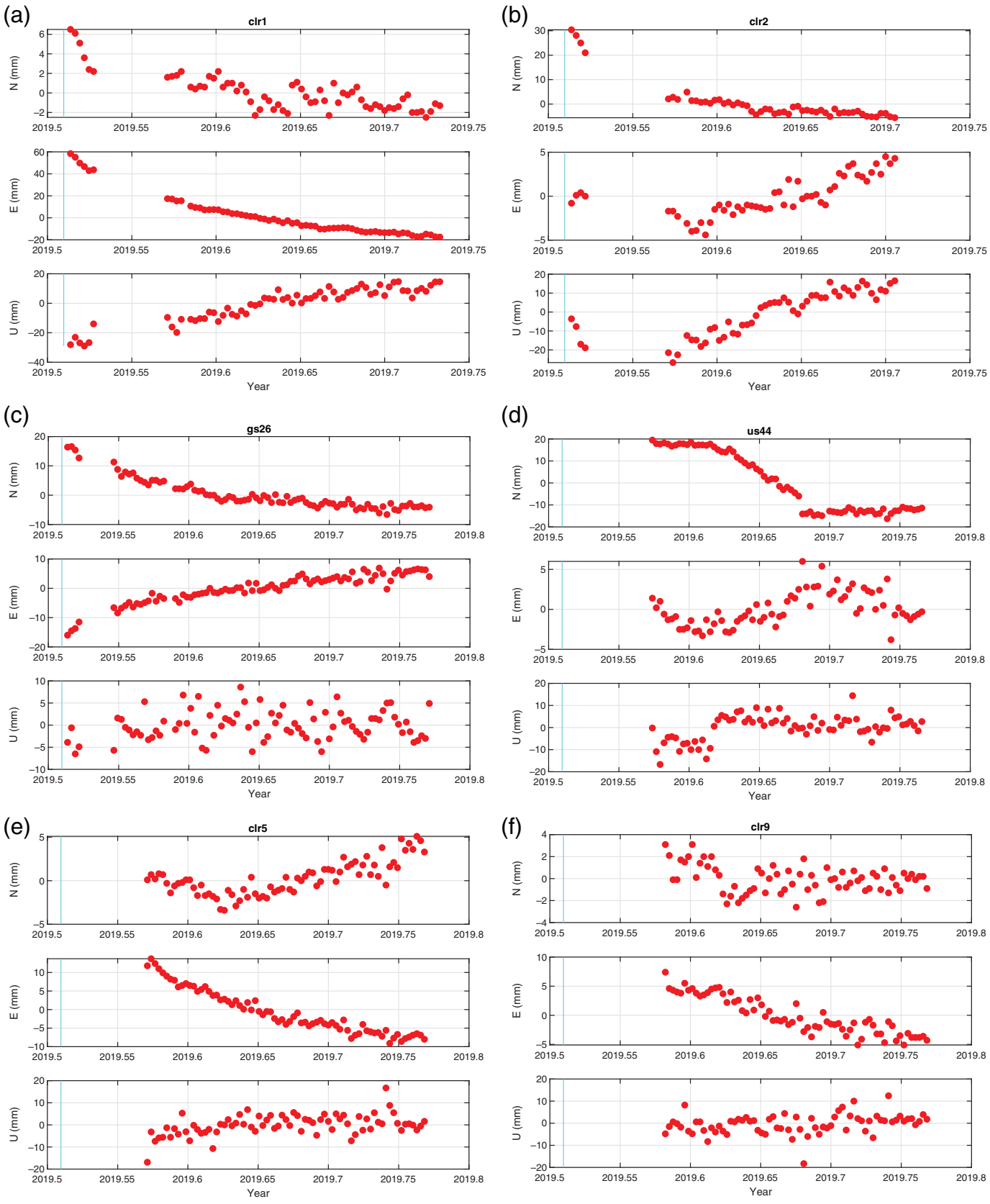

Figure 8. Three-component daily solution time series (north, east, and up) for each station. The vertical cyan line is the date (5 July 2019) of the M_w 7.1 Ridgecrest earthquake. Note different *x*- and *y*-axis scaling for each figure. (a) Station CLR1, (b) station CLR2, (c) station GS26, (d) station US44, (e) station CLR5, and (f) station CLR9.

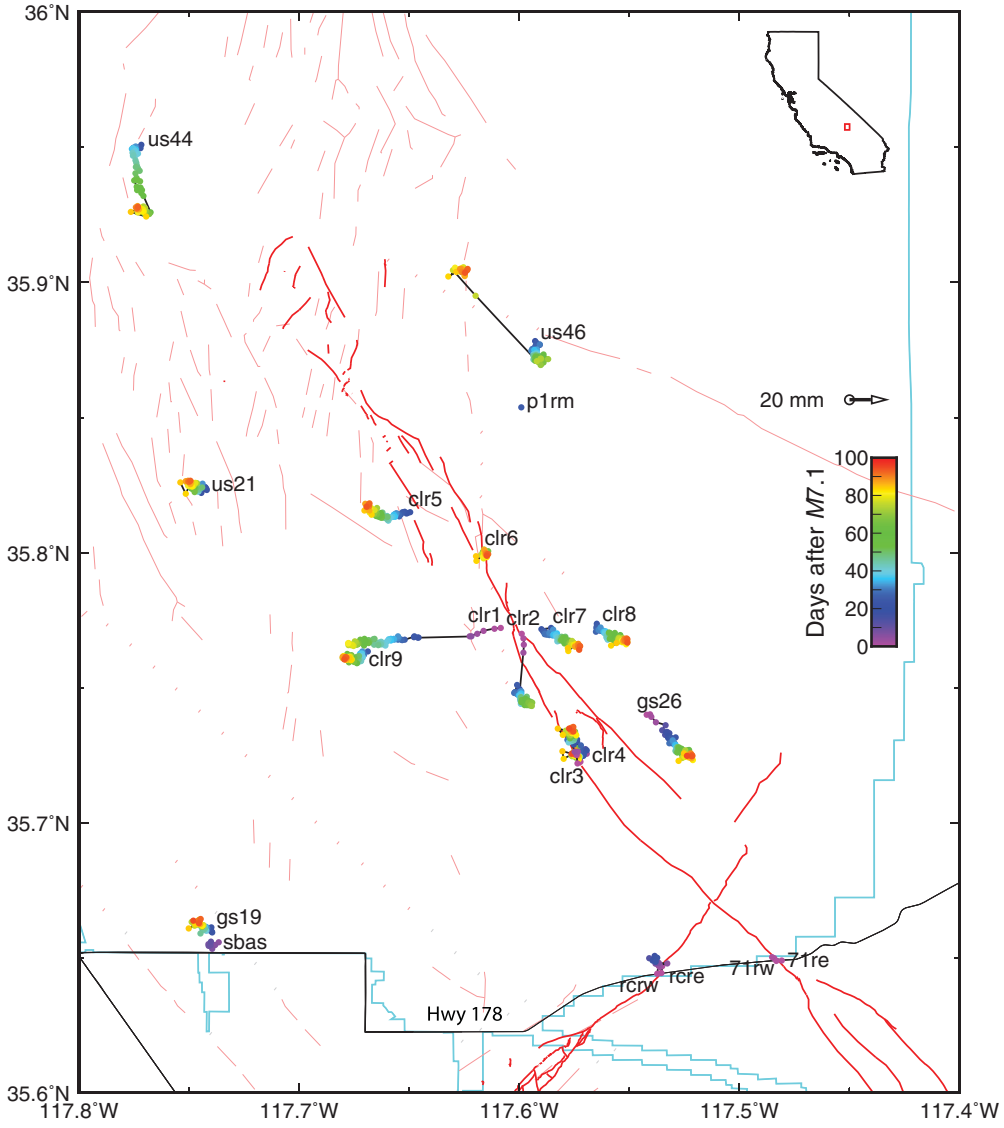

Figure 9. Map of cumulative postseismic displacements for GNSS stations. The circles for each station are color-coded by days after the 5 July *M* 7.1 earthquake. The distance accrued at each time period (represented by an individual circle) is scaled according to the 20 mm vector scale in the legend. Location of the NAWSCL (cyan lines), mapped Quaternary faults (gray lines), the Ridgecrest earthquake sequence surface rupture trace (red lines), and main roads (black lines).

M 7.1 principal plane and the shallow crust surrounding it. We find no evidence for shallow afterslip along the southern quarter of the *M* 7.1 rupture. At Highway 178, the lack of differential motion on the 71RW–71RE baseline (Fig. 7b), combined with no evidence for spray-paint marker offsets, constrains a locked shallow portion of the fault there. This behavior is similar to that near the southern end of the rupture where there is a lack of significant cross-fault motion at creepmeter station R7 (Bilham and Castillo, 2020) (Fig. 1b).

At roughly the midpoint along strike of the *M* 7.1 rupture, however, stations CLR4 (see supplemental material, Fig. 1f) and GS26 (Fig. 8c) on the west and east of the rupture, respectively, show a fault-parallel pattern of displacement consistent with right-lateral shallow afterslip. CLR4 is on the west side of the principal rupture plane, whereas GS26 is on the east side of a major subsidiary strand that accrued ~1 m of right-lateral coseismic displacement in the *M* 7.1 event (C. B. DuRoss *et al.*, unpublished manuscript, see Data and Resources). Station CLR3, however, on the east side of the principal plane, shows no evidence for right-lateral displacement across it. Instead, it manifests a small amount of west-directed fault-normal, cumulative contraction of ~6 mm over ~3 months (Fig. 9). The combination of these three stations' displacement patterns suggests that, at least in this along-strike location, both strands are accruing afterslip and that a relatively stationary sliver of material separates them.

Further to the north by ~6 km, in the epicentral region and the zone of maximum surface displacement (C. B. DuRoss *et al.*, unpublished manuscript, see Data and Resources), the fault-normal displacements exhibited by the west–east trend of stations (CLR9, CLR1, CLR2, CLR7, and CLR8) suggests surface displacements are responding to poroelastic, rather than afterslip, forcing. This pattern of displacements and interpretation of a poroelastic process is also consistent with the postseismic InSAR results (Wang and Bürgmann, 2020) that show a lobe of positive line of sight cumulative displacement, with maximum magnitude ~4 cm over ~2 months, stretching from the epicentral region to the northern limit of the surface rupture (Fig. 5).

The trajectory changes for stations CLR5 (Figs. 8e and 9) and CLR9 (Figs. 8f and 9) to more north-directed, fault-parallel displacements could be evidence for a transition to a surface response more dominated by right-lateral afterslip than poroelastic processes. But the strong, contemporaneous signal at

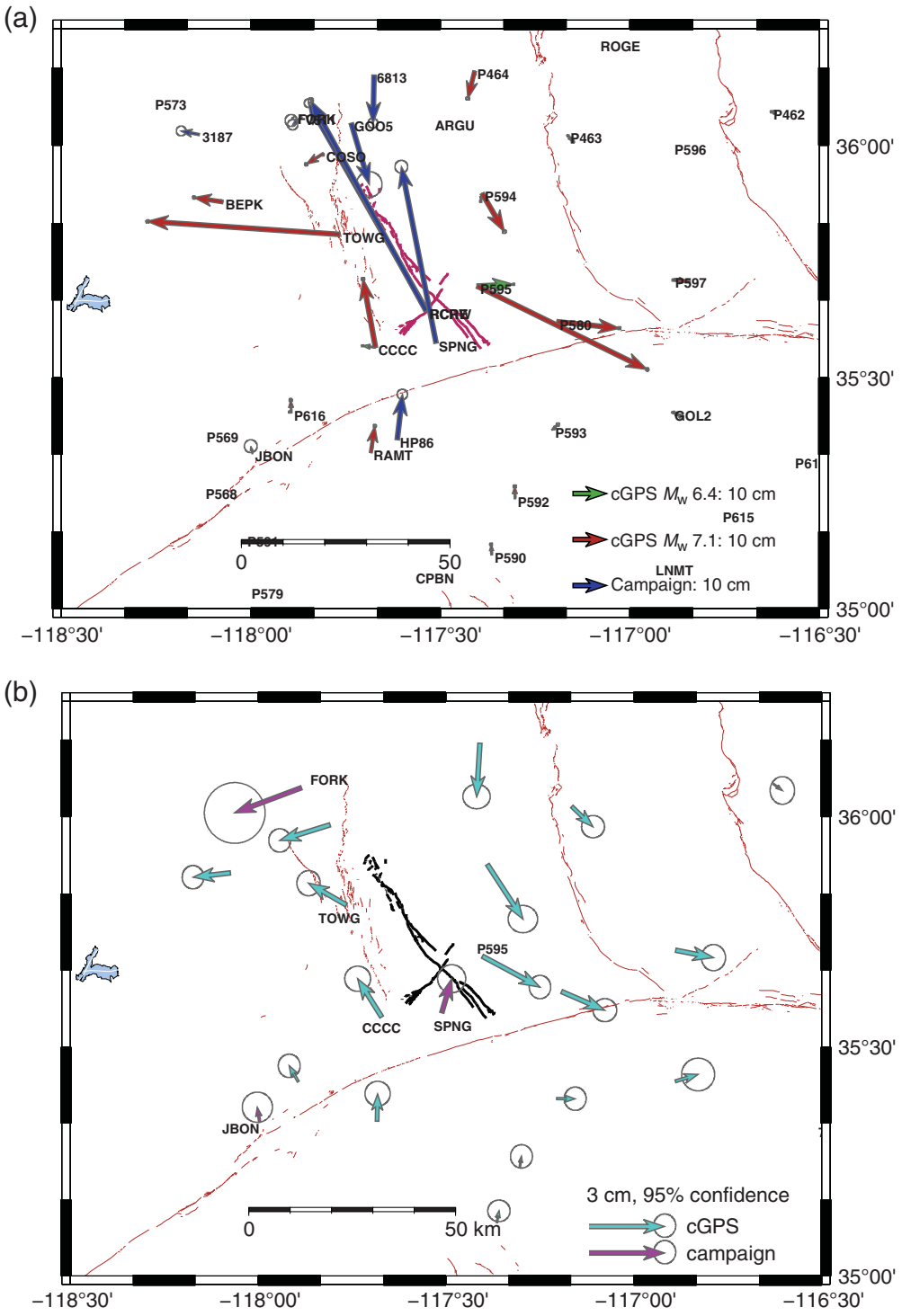

Figure 10. (a) Estimated offsets for M_w 6.4 and 7.1 earthquakes. For campaign data, a single and combined offset is estimated for the two events. (b) Cumulative estimated postseismic motion over first month following 5 July 2019 earthquake. Time series for labeled stations are shown in Figure 2.

station US44, with a transient displacement excursion that is opposite to stations CLR5 and CLR9, although all reside on the same western side of the principal plane, is not consistent with this interpretation. The pattern of surface faulting in this northern termination of the M 7.1 is notable because of the change in faulting style to a series of northeast–southwest-trending cross faults with confirmed normal-faulting displacements (C. B. DuRoss *et al.*, unpublished manuscript, see Data and Resources). Because the displacements are toward one another, however, there is a general contractional state of strain across this zone from US44 in the north to CLR5 and CLR9 to the south. Interpretation of this complicated, time-varying strain field clearly requires further study.

The Effect of the Ridgecrest Earthquakes on Automated Daily GNSS Analysis

The USGS ESC's automated GNSS data processing and time-series analysis system is described in Murray and Svarc (2017). As noted in the Introduction, we apply regional filtering to reduce common mode noise in the time series. We then use the methodology of Langbein and Bock (2004) to estimate velocities, offsets, postseismic, and seasonal motion. To investigate the effect of the Ridgecrest events on our regional filtering and velocity estimation, we first quantify the magnitude of the earthquake-induced signals by computing coseismic and postseismic displacements for continuous stations comprising our "LongValley" region, which spans a geographic area that includes Long Valley, the Ridgecrest source area, and the ECSZ (Figs. 10 and 11). We also present displacement estimates for near-source campaign GPS sites for which USGS has a history of pre-earthquake surveys. To avoid potential bias, regional filtering has not been applied to the

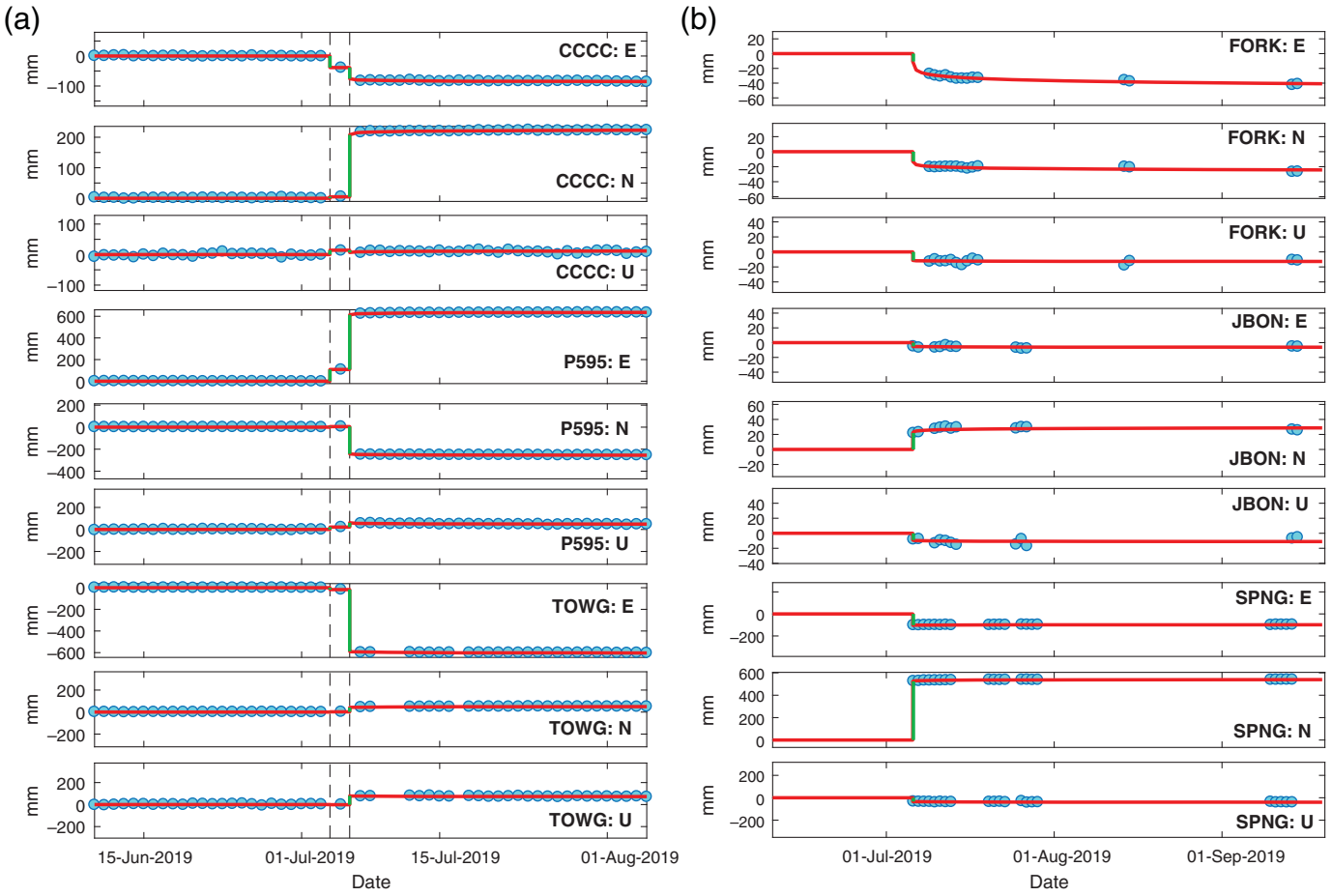

Figure 11. Example time series. Estimated secular rate and (for continuous stations) seasonal terms have been removed. Blue circles denote observations; red lines denote predicted position (coseismic and postseismic) using estimated model parameters; and green lines highlight coseismic offsets. *Y*-axis range is the same for all three components at each station but differs from station-to-station. Station locations marked on Figure 1. (a) Continuous Global Positioning System (GPS) (cGPS) stations and (b) campaign stations.

time series from which these offsets were estimated. For continuous stations, we estimated coseismic offsets at the time of the M_w 6.4 and 7.1 earthquakes and the magnitude of a single logarithmic decay term beginning just after the M_w 7.1 earthquake to account for postseismic motion due to both events. The campaign stations do not have data between the two earthquakes, so we estimate a single offset at the time of the M_w 7.1 earthquake. Three campaign stations operated in quasi-continuous mode after initial deployment, providing sufficient data to estimate the amplitude of postseismic displacement decay following the same approach as with the permanent GPS stations.

Some of the stations used to define the original "LongValley" regional filter experienced earthquake displacements (Fig. 12). Because the regional filtering approach (Blewitt *et al.*, 2013) assumes linear time series, in the days after the earthquake many data points from the filter stations are discarded as outliers. In the longer term, ongoing nonlinear postseismic motion can bias results. Here, we present a preliminary comparison of velocities computed using the original set of filter stations and those calculated using an alternative set of stations, selected for their long and relatively steady motion (Fig. 13). In both cases, we calculate the velocities using data up until 3 July 2019. Generally, small but spatially systematic differences exist between the two velocity fields, which we attribute to the different spatial coverage of the stations used to define the two filters. The alternative set of stations spans a broader geographic area with deformation patterns that differ from that spanned by the original set of stations. Furthermore, southern California GPS time series have been shown to include a common-mode seasonal signal (Langbein, 2008), which is less effectively removed by a filter that spans a broader region.

Generally, as time passes, it becomes increasingly difficult to identify GPS stations with long observation histories that are free of time-varying motion. Thus, it is necessary to correct for the nonlinear signals evident in time series before using them to define a regional filter. One strategy to address earthquake-related displacements such as those affecting stations in the Ridgecrest area is to use models of coseismic slip and postseismic response (e.g., afterslip, poroelastic, and/or viscoelastic

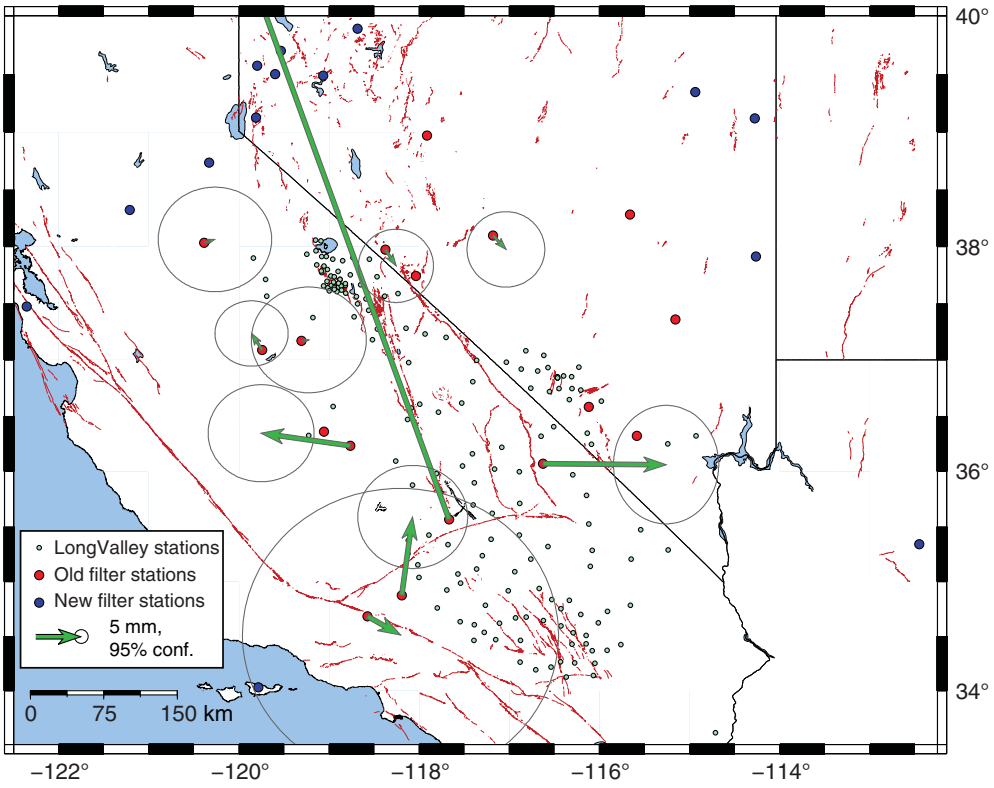

Figure 12. Estimated coseismic offsets at the original set of stations used to define the regional filter. Offsets are the sum of displacements due to the 4 July 2019 M_w 6.4 and 6 July 2019 M 7.1 events.

deformation) to predict and remove these signals. Another approach is to analyze individual time series using the method described previously to estimate coseismic offsets and logarithmic decay, and use these to correct the time series.

Regardless of method, any model adjustment involves implicit assumptions that introduce an additional layer of epistemic uncertainty and potential bias. We further explore the latter approach by assessing the difference between velocities calculated using only the pre-earthquake portion of the time series and velocities estimated simultaneously with coseismic and postseismic terms from the full time series. We carried out this comparison for 21 permanent GPS stations within 75 km of the M_w 7.1 epicenter using data without regional filtering and find that the maximum magnitude of the three-component vector difference in velocity is 0.8 mm/yr and the median is 0.1 mm/yr. That the velocity differences are small is not surprising because the portion of the time series affected by the Ridgecrest events is short relative to the total time-series length. However, long-term postseismic deformation has the potential to bias future velocity estimates, if not well approximated by the assumed functional form (here, logarithmic decay). For example, many stations in the southern portion of our study region were installed in the years following the M_w 7.1 1999 Hector Mine earthquake and were affected by 2010 El Mayor–Cucapah earthquake postseismic deformation, making it difficult to effectively separate postseismic trends from the background secular rate. Poorly modeled long-term postseismic deformation due to these earthquakes contributes to the large observed velocity differences at some stations in Figure 13.

Summary

- In response to the July 2019 Ridgecrest earthquake sequence, we established or reoccupied 24 GNSS sites, 14 of which are on the NAWSCL and, as of this writing, operating continuously.
- Stations RCRW and RCRE were recording a 200 m cross-rupture aperture on 4 July, ~10 hr after the *M* 6.4 event, and they recorded the coseismic displacements of the *M* 7.1. They did not record any post *M* 6.4 shallow afterslip.
- On 5 July, ~1 hr after the *M* 7.1 event stations 71RW and 71RE were recording an ~200 m cross-rupture aperture of the surface rupture. They did not record any post *M* 7.1 shallow afterslip for at least 3–5 days.
- From 6 July to 1 August, we established the rest of the stations ranging to a distance of ~15 km from the *M* 7.1 principal rupture trace. The postseismic time series from these stations show centimeters of horizontal displacement over periods of a few months. They record a mixture of fault-parallel and fault-normal displacements that, in conjunction with analysis of more spatially complete InSAR displacement fields, suggest that both poroelastic and afterslip phenomena occur along the *M* 7.1 rupture plane.
- Using preliminary data from these and other regional stations, we find that redefining a filter using different GNSS stations that are unaffected by the earthquakes results in small, but systematic differences in the regional velocity field estimate.

Data and Resources

All data are available as part of the UNAVCO archive (doi: 10.7283/CNFM-NK42 and available at https://www.unavco.org/data/doi/10.7283/CNFM-NK42). The information about U.S. Geological Survey Earthquake Notification System (USGS-ENS) is available at

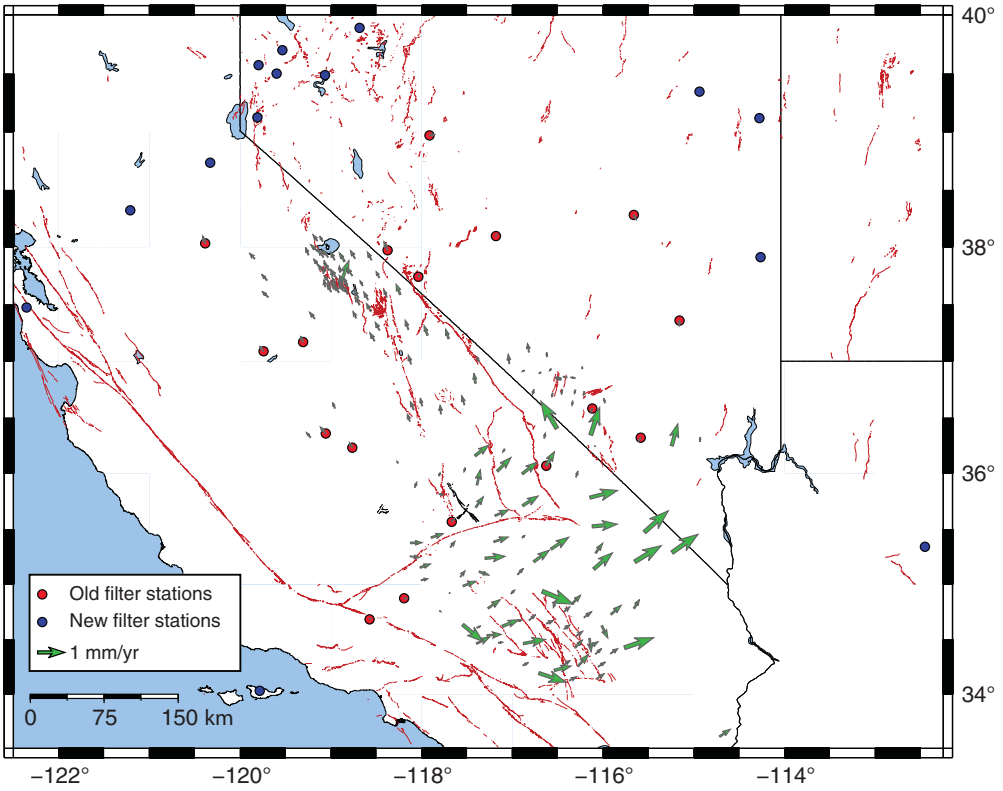

Figure 13. Difference in velocities computed using two different sets of stations to define a regional filter. Velocities are calculated using data up until 3 July 2019 to avoid the effects of the Ridgecrest earthquakes.

https://earthquake.usgs.gov/ens/. The information about California Earthquake Clearinghouse is available at http://californiaeqclearinghouse.org/. These websites were last accessed in March 2020. The supplemental material contains three-component displacement time-series plots for stations not displayed in Figure 8. The unpublished manuscript by C. B. DuRoss, R. Gold, T. Dawson, K. Scharer, K. Kendrick, S. Akciz, S. Angster, S. Bacon, S. Bennett, L. Blair, *et al.* "Surface displacement distributions for the July 2019 Ridgecrest, California earthquake ruptures," submitted to Bull. Seismol. Soc. Am.

Acknowledgments

The authors gratefully acknowledge Naval Air Weapons Station (NAWS) China Lake base commander Paul Dale for permission to access China Lake Naval Air Weapons Station base (NAWSCL) during a critical post-earthquake period for the base. The authors also gratefully acknowledge the tireless and good-natured field support of Stephan Bork (Water Quality Program NAWS China Lake) and Bill Willard NAWS China Lake. The authors thank the California National Guard for helicopter field support. The authors thank Matt Boggs, Margo Allen, and Helen Haase of NAWS China Lake for further logistical support. The authors thank Margaret Benoit and Luciana Astiz of the National Science Foundation (NSF) for facilitating our request for Global Navigation Satellite System (GNSS) equipment support. The authors thank Glen Matioli and Joe Petit of UNAVCO for expediting our request for instrument support.

Any use of trade, firm, or product names is for descriptive purposes only and does not imply endorsement by the U.S. government.

References

Aagaard, B. T., J. J. Lienkaemper, and D. P. Schwartz (2012). Probabilistic estimates of surface coseismic slip and afterslip for Hayward fault earthquakes, *Bull. Seismol. Soc. Am.* **102,** 961–979.

Becker, T. W., J. L. Hardebeck, and G. Anderson (2005). Constraints on fault slip rates of the southern California plate boundary from GPS velocity and stress inversions, *Geophys. J. Int.* **160,** 634–650.

Bilham, R. (2005). Coseismic strain and the transition to surface afterslip recorded by creepmeters near the 2004 Parkfield epicenter, *Seismol. Res. Lett.* **76,** 49–57.

Bilham, R., and B. Castillo (2020). The July 2019 Ridgecrest, California, earthquake sequence recorded by creepmeters: Negligible epicentral afterslip and prolonged triggered slip at teleseismic distances, *Seismol. Res. Lett.* doi: 10.1785/0220190293.

Blewitt, G., C. Kreemer, W. C. Hammond, and J. M. Goldfarb (2013). Terrestrial reference frame NA12 for crustal deformation studies in North America, *J. Geodyn.* **72,** 11–24.

Brooks, B. A., S. E. Minson, C. L. Glennie, J. M. Nevitt, T. Dawson, R. S. Rubin, T. L. Ericksen, D. Lockner, K. Hudnut, V. Langenheim, *et al.* (2017). Buried shallow fault slip from the South Napa earthquake revealed by near-field geodesy, *Sci. Adv.* **3,** doi: 10.1126/sciadv.1700525.

Bürgmann, R., and G. Dresen (2008). Rheology of the lower crust and upper mantle: Evidence from rock mechanics, geodesy, and field observations, *Annu. Rev. Earth Planet. Sci.* **36,** 531–567.

Dolan, J. F., and B. D. Haravitch (2014). How well do surface slip measurements track slip at depth in large strike-slip earthquakes? The importance of fault structural maturity in controlling on-fault slip versus off-fault surface deformation, *Earth Planet. Sci. Lett.* **388,** 38–47.

Fialko, Y., D. Sandwell, M. Simons, and P. Rosen (2005). Three-dimensional deformation caused by the Bam, Iran, earthquake and the origin of shallow slip deficit, *Nature* **435,** 295–299.

Floyd, M., G. Funning, Y. Fialko, R. Terry, and T. Herring (2020). Survey and continuous GNSS in the vicinity of the July 2019 Ridgecrest earthquakes, *Seismol. Res. Lett.* doi: 10.1785/0220190324.

Floyd, M. A., R. J. Walters, J. R. Elliott, G. J. Funning, J. L. Svarc, J. R. Murray, A. J. Hooper, Y. Larsen, P. Marinkovic, R. Bürgmann, *et al.*

(2016). Spatial variations in fault friction related to lithology from rupture and afterslip of the 2014 South Napa, California, earthquake, *Geophys. Res. Lett.* **43,** 6808–6816.

Hudnut, K. W., B. Brooks, K. Scharer, J. L. Hernandez, T. E. Dawson, M. E. Oskin, R. Arrowsmith, K. Blake, M. L. Boggs, S. Bork, *et al.* (2020). Airborne lidar and electro-optical imagery along surface ruptures of the 2019 Ridgecrest earthquake sequence, Southern California, *Seismol. Res. Lett.* doi: 10.1785/0220190338.

Langbein, J. (2008). Noise in GPS displacement measurements from southern California and southern Nevada, *J. Geophys. Res.* **113,** doi: 10.1029/2007JB005247.

Langbein, J., and Y. Bock (2004). High-rate real-time GPS network at Parkfield: Utility for detecting fault slip and seismic displacements, *Geophys. Res. Lett.* **31,** doi: 10.1029/2003GL019408.

Langbein, J., J. Murray, and H. Snyder (2006). Coseismic and initial postseismic deformation from the 2004 Parkfield, California, earthquake, observed by Global Positioning System, electronic distance meter, creepmeters, and borehole strainmeters, *Bull. Seismol. Soc. Am.* **96,** S304–S320.

Lienkaemper, J. J., S. B. DeLOng, C. Domrose, and C. M. Rosa (2016). Afterslip behavior following the 2014 M 6.0 South Napa Earthquake with implications for afterslip forecasting on other seismogenic fault, *Seismol. Res. Lett.* doi: 10.1785/0220150262.

Marone, C. J., C. H. Scholz, and R. Bilham (1991). On the mechanics of earthquake afterslip, *J. Geophys. Res.* **96,** 8441–8452.

Milliner, C. W. D., J. F. Dolan, J. Hollingsworth, S. Leprince, F. Ayoub, and C. G. Sammis (2015). Quantifying near-field and off-fault deformation patterns of the 1992 Mw 7.3 Landers earthquake, *Geochem. Geophys. Geosys.* **16,** doi: 10.1002/2014GC005693.

Murray, J. R., and J. Svarc (2017). Global Positioning System data collection, processing, and analysis conducted by the U.S. Geological Survey Earthquake Hazards Program, *Seismol. Res. Lett.* **88,** 916–925.

Nissen, E., T. Maruyama, J. Ramon Arrowsmith, J. R. Elliott, A. K. Krishnan, M. E. Oskin, and S. Saripalli (2014). Coseismic fault zone deformation revealed with differential lidar: Examples from Japanese M ∼ 7 intraplate earthquakes, *Earth Planet. Sci. Lett.* **405,** 244–256.

Peltzer, G., P. Rosen, F. Rogez, and K. Hudnut (1996). Postseismic rebound in fault step-overs caused by pore fluid flow, *Science* **273,** 1202–1204.

Petersen, M. D., T. E. Dawson, R. Chen, T. Cao, C. J. Wills, D. P. Schwartz, and A. D. Frankel (2011). Fault displacement hazard for strike-slip faults, *Bull. Seismol. Soc. Am.* **101,** 805–825.

Pollitz, F. F., C. Wicks, and W. Thatcher (2001). Mantle flow beneath a continental strike-slip fault: Postseismic deformation after the 1999 Hector Mine earthquake, *Science* **293,** 1814–1818.

Ross, Z. E., B. Idini, Z. Jia, O. L. Stephenson, M. Zhong, X. Wang, Z. Zhan, M. Simons, E. J. Fielding, and S.-H. Yun (2019). Hierarchical interlocked orthogonal faulting in the 2019 Ridgecrest earthquake sequence, *Science* **366,** 346–351.

Simons, M., Y. Fialko, and L. Rivera (2002). Coseismic deformation from the 1999 Mw 7.1 Hector Mine, California, earthquake as inferred from InSAR and GPS observations, *Bull. Seismol. Soc. Am.* **92,** 1390–1402.

Stewart, J. P., S. Brandenberg, P. Wang, C. Chukwuebuka, K. Hudson, S. Mazzoni, Y. Bozorgnia, K. Hudnut, and C. Davis (2019). Preliminary Report on Engineering and Geological Effects of the July 2019 Ridgecrest Earthquake Sequence, *Geotechnical Extreme Event Reconnaissance Association Rept. GEER 64*, doi: 10.18118/G6H66K.

Wang, K., and R. Bürgmann (2020). Co-and early postseismic deformation due to the 2019 Ridgecrest earthquake sequence constrained by Sentinel-1 and COSMO-SkyMed SAR data, *Seismol. Res. Lett.* doi: 10.1785/0220190299.

Wesnousky, S. G. (2008). Displacement and geometrical characteristics of earthquake surface ruptures: Issues and implications for seismic-hazard analysis and the process of earthquake rupture, *Bull. Seismol. Soc. Am.* **98,** 1609–1632.

Xu, X., X. Tong, D. T. Sandwell, C. W. D. Milliner, J. F. Dolan, J. Hollingsworth, S. Leprince, and F. Ayoub (2016). Refining the shallow slip deficit, *Geophys. J. Int.* **204,** 1843–1862.

Zinke, R., J. Hollingsworth, and J. F. Dolan (2014). Surface slip and off-fault deformation patterns in the 2013 MW 7.7 Balochistan, Pakistan earthquake: Implications for controls on the distribution of near-surface coseismic slip, *Geochem. Geophys. Geosys.* **15**.

Manuscript received 7 January 2020
Published online 27 May 2020